ACS APPLIED MATERIALS & INTERFACES

www.acsami.org Research Article

# Control-Etched $Ti_3C_2T_x$ MXene Nanosheets for a Low-Voltage-Operating Flexible Memristor for Efficient Neuromorphic Computation

Jeny Gosai, Mansi Patel, Lingli Liu, Aziz Lokhandwala, Parth Thakkar, Mun Yin Chee, Muskan Jain, Wen Siang Lew, Nitin Chaudhari,* and Ankur Solanki*

Cite This: ACS Appl. Mater. Interfaces 2024, 16, 17821−17831

Read Online

ACCESS | Metrics & More | Article Recommendations | Supporting Information



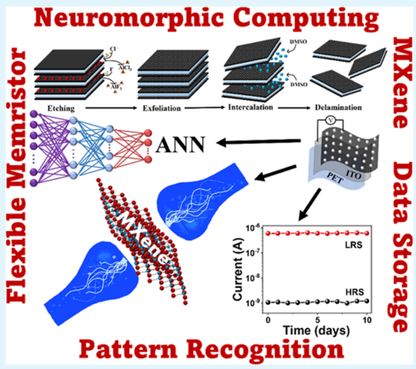


**ABSTRACT:** Hardware neural networks with mechanical flexibility are promising next-generation computing systems for smart wearable electronics. Overcoming the challenge of developing a fully synaptic plastic network, we demonstrate a low-operating-voltage PET/ITO/p-MXene/Ag flexible memristor device by controlling the etching of aluminum metal ions in $Ti_3C_2T_x$ MXene. The presence of a small fraction of Al ions in partially etched MXene (p-$Ti_3C_2T_x$) significantly suppresses the operating voltage to 1 V compared to 7 V from fully Al etched MXene (f-$Ti_3C_2T_x$)-based devices. Former devices exhibit excellent non-volatile data storage properties, with a robust $\sim 10^3$ ON/OFF ratio, high endurance of $\sim 10^4$ cycles, multilevel resistance states, and long data retention measured up to $\sim 10^6$ s. High mechanical stability up to ~73° bending angle and environmental robustness are confirmed with consistent switching characteristics under increasing temperature and humid conditions. Furthermore, a p-$Ti_3C_2T_x$ MXene memristor is employed to mimic the biological synapse by measuring the learning−forgetting pattern for $\sim 10^4$ cycles as potentiation and depression. Spike time-dependent plasticity (STDP) based on Hebb's Learning rules is also successfully demonstrated. Moreover, a remarkable accuracy of ~95% in recognizing modified patterns from the National Institute of Standards and Technology (MNIST) data set with just 29 training epochs is achieved in simulation. Ultimately, our findings underscore the potential of MXene-based flexible memristor devices as versatile components for data storage and neuromorphic computing.

**KEYWORDS:** *flexible memristor, MXene, resistive switching, artificial synapse, neuromorphic computation, MNIST*

## 1. INTRODUCTION

Memristors have gained more attention than the traditional von Neumann architecture because of their high efficiency, low power consumption, flexible and parallel signal processing.[1,2] Due to their non-volatile nature, they can retain their resistance states on withdrawal of power, making them ideal for storage applications.[3,4] High switching speeds, low energy consumption, and scalability have also positioned memristors as potential candidates for neuromorphic computing, where they can emulate the synaptic behavior of biological neurons.[5] Furthermore, memristors offer possibilities for analog computing,[6] in-memory computing,[7] and even unconventional computing paradigms like reservoir computing.[8] Synapses and neurons are the basic building blocks of the neuromorphic architecture, where pre- and post-synaptic neurons interact via synapses. The ionic influx of $Na^+$ and $Ca^{2+}$ via neurons modifies the synaptic weight.[9] In artificial synaptic devices, memristors can assist in simulating the functionalities of biological synapses.[10] Memristor performance is based on conductance measurements.[11] The difference in synaptic weights between pre-synaptic and post-synaptic neurons determines a progressive change in conductance.[12]

Recently, research in the field of memristors is undergoing rapid advancements as scientists delve into novel materials, device architectures, and fabrication techniques to enhance performance and reliability. Various types of memristors based on oxides,[13,14] transition metal dichalcogenides (TMDCs),[15] organics,[16] composites,[17] perovskites,[18,19] metal halides,[20] and non-Newtonian fluids[21] materials[22] are being explored, with each offering unique characteristics and potential applications. To fully harness their potential and enable practical implementations in memory and computing systems, the development of memristor-based crossbar arrays and integrated circuits is crucial.[23] In recent years, two-dimensional

Received: January 24, 2024
Revised: March 6, 2024
Accepted: March 11, 2024
Published: March 27, 2024

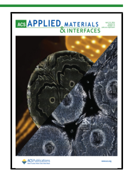

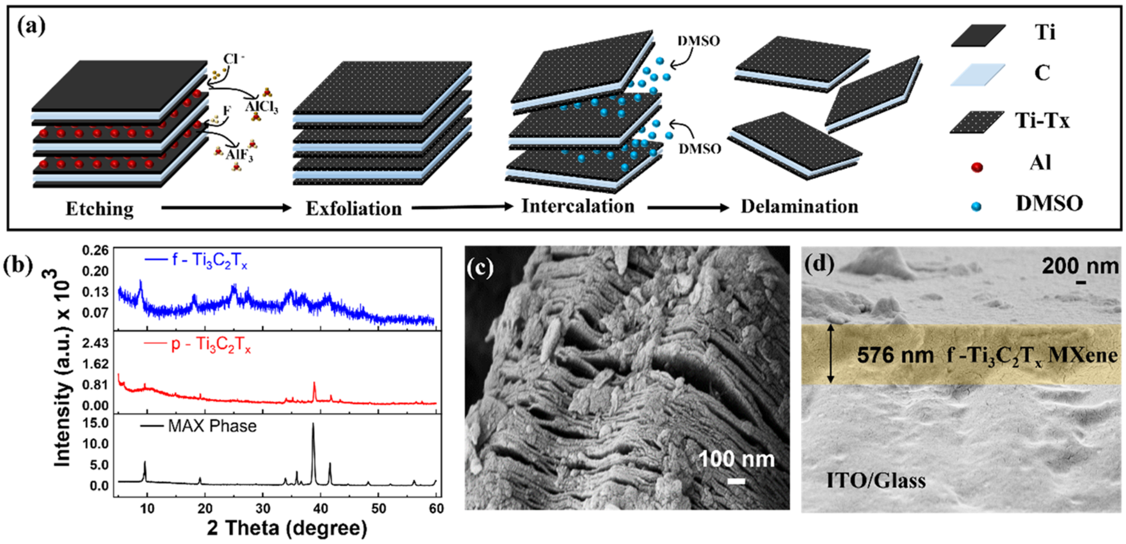


**Figure 1.** (a) Schematic of the synthesis of 2D $Ti_3C_2T_x$ MXene and delamination of the exfoliated sheets. (b) XRD analysis of MAX phase, 2D p- and f-$Ti_3C_2T_x$ MXene. (c) Field emission scanning electron microscopy (FE-SEM) image of the $Ti_3C_2T_x$ powder, (d) Cross-sectional FE-SEM image of the f-$Ti_3C_2T_x$ thin film coated on an indium tin oxide (ITO) glass substrate.

(2D) nanomaterials have emerged as a promising class of materials for brain-like computing systems.[5] Among various 2D materials, MXene nanosheets have garnered significant attention. In general, MXenes are 2D transition metal carbides, nitrides, or carbonitrides with the formula $M_{n+1}X_nT_x$, where M represents an early transition metal, X is carbon or nitrogen, $T_x$ is the surface termination groups, and $n$ = 1−4.[24] MXene exhibits properties that make them well-suited for use in memristors, which include tunable conductivity, and excellent chemical stability.[25] MXenes can be synthesized from precursor MAX phases by selectively removing the aluminum (Al) layer.[26] Furthermore, $Ti_3C_2T_x$ MXene, in particular, has found extensive applications in various fields such as actuators,[27] sensors,[28] electromagnetic interference shielding,[29] supercapacitors,[30] batteries,[31] catalysts,[32] solar cells,[33] and more.[34,35] The versatile properties and wide range of applications make $Ti_3C_2T_x$ MXene an emerging material for research and development. Overall, ongoing research aims to push the boundaries of memristor technology through the exploration of novel materials like MXenes as well as the optimization of device architectures and fabrication techniques. These advancements pave the way for innovative applications in memory,[36] computing and other diverse fields.

Herein, we demonstrate that $Ti_3C_2T_x$ MXene-based flexible artificial synapses emerge as a promising candidate for brain-inspired computing and data storage applications. Notably, the research pioneers an in-depth analysis of the mechanical performance of flexible memristor devices under ambient conditions without encapsulation, revealing robustness at a ~73° bending angle. Multilevel retention and controlled etching further contribute to the appeal of these devices, showcasing low energy consumption and reduced operational voltage. The in-depth investigation encompasses a comprehensive exploration of data storage metrics such as ON/OFF ratio (~$10^3$), endurance (measured ~$10^4$ cycles), retention (measured up to ~$10^6$ s (10 days)), top electrode variation, and bending-angle variations. Temperature- and relative humidity-dependent retention measurements demonstrate negligible degradation in resistance states, attesting to the reliability of the $Ti_3C_2T_x$ MXene-based devices. Further investigation also reveals a remarkable consistency in potentiation and depression cycles, even under bending conditions. Moreover, we demonstrate the implementation of spike time-dependent plasticity based on Hebbian learning rules and the achievement of a notable ~95% accuracy in modified patterns from the National Institute of Standards and Technology (MNIST) pattern recognition after only 29 epochs via simulation. This underscores the immense potential of $Ti_3C_2T_x$ MXene-based devices in advancing the field of flexible data storage and brain-inspired computing.

## 2. RESULTS AND DISCUSSION

**2.1. Structural Analysis.** Schematic representation of synthesized multilayer $Ti_3C_2T_x$ MXene nanosheets from their precursor $Ti_3AlC_2$ MAX phase is shown in Figure 1a. The etching reagents used to selectively etch the Al layer were a mixture of hydrochloric acid (HCl) and lithium fluoride (LiF) to generate *in situ* hydrofluoric acid (HF). The selective etching of the Al layer is possible because of the weaker connection between Ti−Al as compared to the Ti−C, which binds the whole structure together. Delamination of this multilayered structure into a few-layered $Ti_3C_2T_x$ MXene nanosheets involves intercalation to separate the nanosheets. Deionized water (DI water) and dimethyl sulfoxide (DMSO) were used as intercalants. Through UV−vis spectroscopy, it was observed that through delamination in DI water, the $Ti_3C_2T_x$ MXene nanosheets were oxidized as an absorption peak of $TiO_x$ was found (Figure S1a) whereas DMSO as a delaminating agent does not show any absorption peak. DMSO is considered the most effective intercalant to delaminate MXene nanosheets. X-ray diffraction (XRD) analysis validates the synthesis of $Ti_3C_2T_x$ MXene, which is partial in the case of *in situ* HF, whereas it has been fully etched when HF is directly used as an etching agent (Figure 1b). The MAX phase shifts from crystalline to amorphous as the Al is completely etched from $Ti_3C_2T_x$ MXene (f-$Ti_3C_2T_x$), whereas the partially etched $Ti_3C_2T_x$ MXene (p-$Ti_3C_2T_x$) represents partial crystallinity due to the presence of Al (~8%). The intensity of the 39° peak (104) has been significantly decreased compared to the $Ti_3AlC_2$ MAX phase when *in situ* HF was


https://doi.org/10.1021/acsami.4c01364
ACS Appl. Mater. Interfaces 2024, 16, 17821−17831

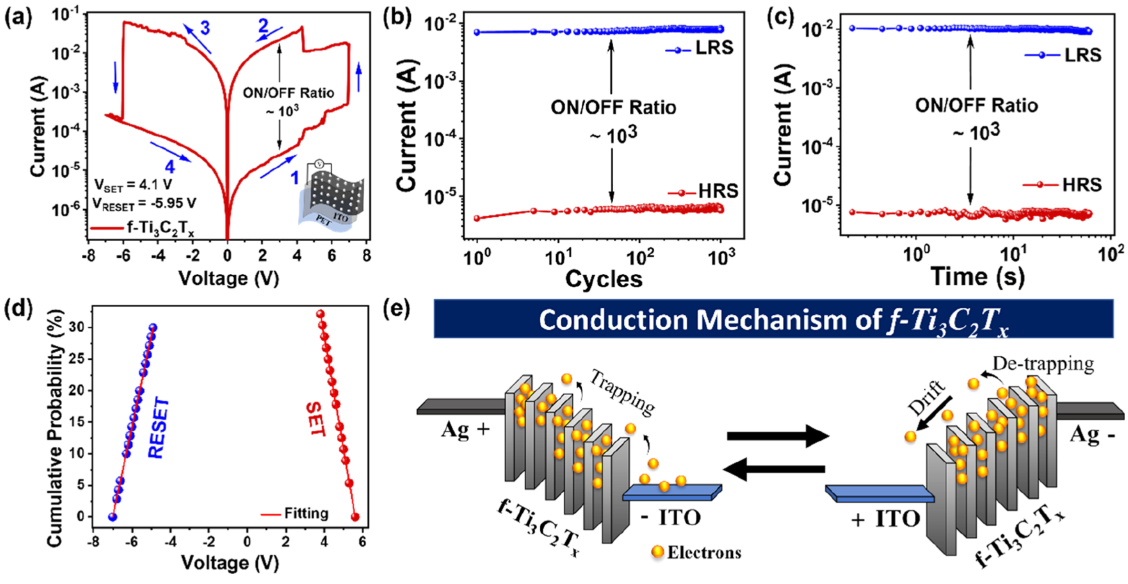


**Figure 2.** Characteristic of 2D f-$Ti_3C_2T_x$ MXene-based memristor. (a) *I*−*V* characteristic of 2D f-$Ti_3C_2T_x$ MXene-based memristor at an operating voltage cycle of 0 V → +7 V → 0 V → −7 V → 0 V. (b) Endurance at an input pulse of 3 V/1 ms. (c) Retention with input pulse applied +3 V → +0.5 (read voltage) → −3 V → +0.5 V (read voltage). (d) Cumulative probability of SET and RESET voltage. (e) Illustration of the conduction mechanism.

used; on the other hand, the 39° peak (104) has completely vanished in the case of HF as an etchant. Also, in f-$Ti_3C_2T_x$, the peak (002) has shifted from 9 to 8°, signifying the increase in interlayer distance between the two sheets; however, p-$Ti_3C_2T_x$ shows just the widening of bump, signifying that the interlayer distance has not been as expanded comparatively.[37] It was observed to be 0.05% in the HF-etched $Ti_3C_2T_x$ MXene, whereas in the case of *in situ* HF, it was around 8%.

The morphology of MXene sheets was characterized by field emission scanning electron microscopy (FE-SEM), which verifies the classic accordion-like structure with a flat surface and an opened interspace of the multilayered MXene nanosheets as shown in Figure 1c. The SEM image confirms the complete removal of Al from the MAX phase (Figure S2a), as there are sheet-like structures all over the synthesized MXene material. During the etching process, the Ti−C bonds are formed, and the Ti−Al bonds get broken. Hence, to stabilize these newly formed bonds, certain functional groups attach themselves to the surface of the nanosheets known as surface terminations.[38] These surface terminations are held responsible for many properties, such as hydrophilicity and conductance. From Fourier transform infrared spectra (FT-IR), the surface termination scan is determined. In Figure S1b (Supporting Information), FT-IR analysis of the p-$Ti_3C_2T_x$ MXene displays the reflections at 3424, 1407, 1007, and 687 $cm^{-1}$, which correspond to the −OH, −H, −F, and −Cl functional groups. The cross-sectional FE-SEM provides the film thickness of a 576 nm f-$Ti_3C_2T_x$ active layer and an 185 nm of p-$Ti_3C_2T_x$ MXene film (Figures 1c and S2b, respectively).

**2.2. Electrical Performance.** The memristor devices comprising the structure PET/ITO/f-$Ti_3C_2T_x$/Ag were prepared on indium tin oxide (ITO) coated poly(ethylene terephthalate) (PET) flexible substrates. Figure 2a demonstrates the resistive switching (RS) characteristics of the memristor device by applying a voltage sweep in the sequence of 0 V → +7 V → 0 V → −7 V → 0 V under flat conditions. During the forward scan of the applied voltage, devices initially remain in a high-resistance state (HRS) or off state and abruptly switch to a low-resistance state (LRS) or on state via the SET process. The device exhibits SET and RESET voltages of ∼(+4.1) and ∼(−5.9) V, respectively, with a current on/off ratio of ∼$10^3$. The per pulse energy consumption of f-$Ti_3C_2T_x$-based memristor devices is estimated as ∼0.128 $\mu J/mm^2$. Furthermore, the presence of the strong covalent bonds between the transition metal−carbon/nitrogen atoms and the functional groups contribute to the overall stability of the MXene active layer; therefore, devices demonstrate high data endurance measured up to ∼$10^3$ cycles (Figure 2b) with the retention measured up to $10^2$ s (Figure 2c) at 0.5 V read voltage without any significant degradation. The cumulative probability distribution reveals less inconsistency for SET and RESET, showing the uniformity of the device (Figure 2d).

Here, we hypothesize two parallel mechanisms (charge trapping/detrapping and filament formation/rupture) for resistive switching in these devices. First, it is noteworthy that the memristor is a vertical device configuration, where uninterrupted charge transport between the bottom and top electrodes in the on state is recommended for a good ON/OFF ratio. The MAX phase comprises of a layered structure (Figure 1a), and the etching process leads to the depletion of complete Al ions, increasing the interlayer distance during the etching process to obtain the MXene. Further intercalation is done by dimethyl sulfoxide (DMSO) between two consecutive layers of $Ti_3C_2T_x$ to end up in f-$Ti_3C_2T_x$. This spacer intercalant, DMSO, leads to multiple high-energy barriers in f-$Ti_3C_2T_x$ layers sandwiched between top and bottom electrodes by introducing multiple quantum well-type structures, as demonstrated in Figure 2d. At low applied bias voltage, electrons trapped in the quantum well do not have ample energy to cross the energy barrier, and a low current in HRS is observed. As the applied bias increases beyond the threshold voltage, trapped electrons achieve sufficient energy to detrapping and cross the barrier to switching the device into LRS with a high SET voltage. Second, we also demonstrate that the filament formation/rupture of $Ag^+$ ions and oxygen

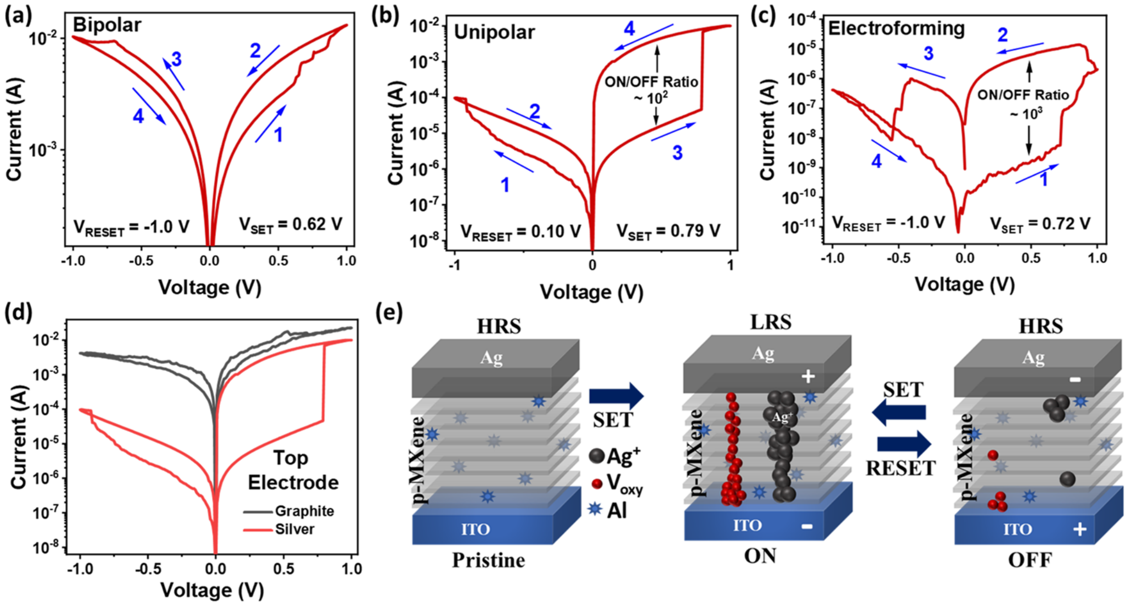


**Figure 3.** Characteristic of 2D p-$Ti_3C_2T_x$ MXene-based memristor $I-V$ characteristics of (a) bipolar, (b) unipolar, (c) electroforming, (d) top electrode variation analysis, and (e) illustration of the conduction mechanism.

vacancies play a crucial role in the conduction mechanism (for a detailed study, please refer to the SI, Figure S3).

High SET/RESET voltage (Figure 2a) disqualifies f-$Ti_3C_2T_x$-based memristor devices for advanced electronic applications, where low energy consumption is the prime requirement. Reducing the interlayer gap between consecutive MXene layers by controlling the etching process is a strategy to lower the SET/RESET voltage and make the structure environmentally and mechanically stable. Devices comprising a p-$Ti_3C_2T_x$ active layer with reduced interlayer gap show a dramatically low SET/RESET voltage as envisaged (Figure 3a). In the absence of the quantum well-type structure owing to the presence of the Al ions between consecutive layers of $Ti_3C_2T_x$ in p-$Ti_3C_2T_x$-based memristor devices, charge trapping/detrapping is suppressed and the RS behavior is dominated by the conducting filament formation/rupture mechanism. This compatibility contributes to the overall improved performance and stability of MXene-based memristors. Herein, partially etched MXene (p-$Ti_3C_2T_x$) demonstrates RS characteristics under a comparatively extremely low operating voltage of 1.0 V. The presence of Al ions in the p-$Ti_3C_2T_x$ layer contributes to the suppression of the operating voltage by reducing the energy barrier between consecutive p-$Ti_3C_2T_x$ layers; therefore, the per pulse low energy consumption of 1.36 nJ/mm$^2$ is estimated compared to 0.128 $\mu$J/mm$^2$ in f-$Ti_3C_2T_x$-based devices. This also resembles the decrease of electric field from $7 \times 10^6$ V/m in f-$Ti_3C_2T_x$ to $4 \times 10^6$ V/m in p-$Ti_3C_2T_x$ MXene-based memristor devices for the SET process.

An intriguing phenomenon is observed as the tunability of RS characteristics between unipolar to bipolar by tuning the polarity of the voltage sweep. The bipolar RS was obtained at positive to negative voltage sweep direction (Figure 3a) with a poor ON/OFF ratio of ~3. By reversing the voltage sweep direction, the RS behavior is changed to unipolar, demonstrating a good ON/OFF ratio of ~$10^2$ (Figure 3b). Here, an electroforming cycle was carried out with voltage transitions from 0 V → +10 V → 0 V (Figure S4a) to achieve the RS. In this process, as shown in Figure 3c, an increase in the ON/OFF ratio (~$10^3$) and a devaluation in per pulse energy consumption of ~0.24 nJ/mm$^2$ is observed compared to 0.128 $\mu$J/mm$^2$ in f-$Ti_3C_2T_x$-based devices (Figure 2a) with a bipolar RS behavior.

The contribution of $Ag^+$ ions for RS is investigated by altering the top electrode to graphite (inactive) instead of Ag (active) (Figure 3c). The poor ON/OFF ratio in graphite-based memristor devices confirms the dominant role of Ag ions instead of oxygen vacancies in RS in p-$Ti_3C_2T_x$. The presence of the Ag top electrode onto MXene surfaces may also form low-resistance interfaces, allowing efficient charge transfer between the electrode and the MXene layer.[25] The general mechanism for resistive switching in PET/ITO/p-$Ti_3C_2T_x$/Ag memristors follows the penetration of $Ag^+$ ions into the p-$Ti_3C_2T_x$ active layer and the migration of oxygen vacancies (Figure 3e). The presence of Al ions bridges consecutive $Ti_3C_2T_x$-layers in the active layer and therefore reduces the series resistance for an efficient ion migration, hence being able to transit in LRS at a lower voltage (for a detailed explanation, please refer to SI, Figures S4b and S5).

The p-$Ti_3C_2T_x$ MXene has demonstrated remarkable memristor performance, showcasing a stable endurance of $10^4$ cycles (Figure 4a). The retention tests conducted over a span of 10 days, equivalent to ~$10^6$ s, reveal the state-of-the-art performance in comparison to the existing $Ti_3C_2T_x$-based memristors (Figure 4b and Table 1). Notably, the device exhibits multilevel retention with up to 25 states, maintaining stable retention for ~$10^3$ s. Temperature-dependent retention investigated at various temperatures (25, 30, 40, 50, 60, 70, and 80 °C) highlights the efficiency of the device at 60 °C. However, a critical observation emerges that the increase in temperatures beyond this point leads to MXene oxidation and subsequent degradation.[52]

Relative humidity (RH)-dependent retention was measured at 40, 50, 60, and 70% for ~$10^3$ s in each state with almost no degradation in the resistance states until 60% RH (Figure 4e).[53] The statistical data suggested the invariant electrical uniformity in the five batch-to-batch characterization measured 50 devices in each batch.


https://doi.org/10.1021/acsami.4c01364
ACS Appl. Mater. Interfaces 2024, 16, 17821−17831

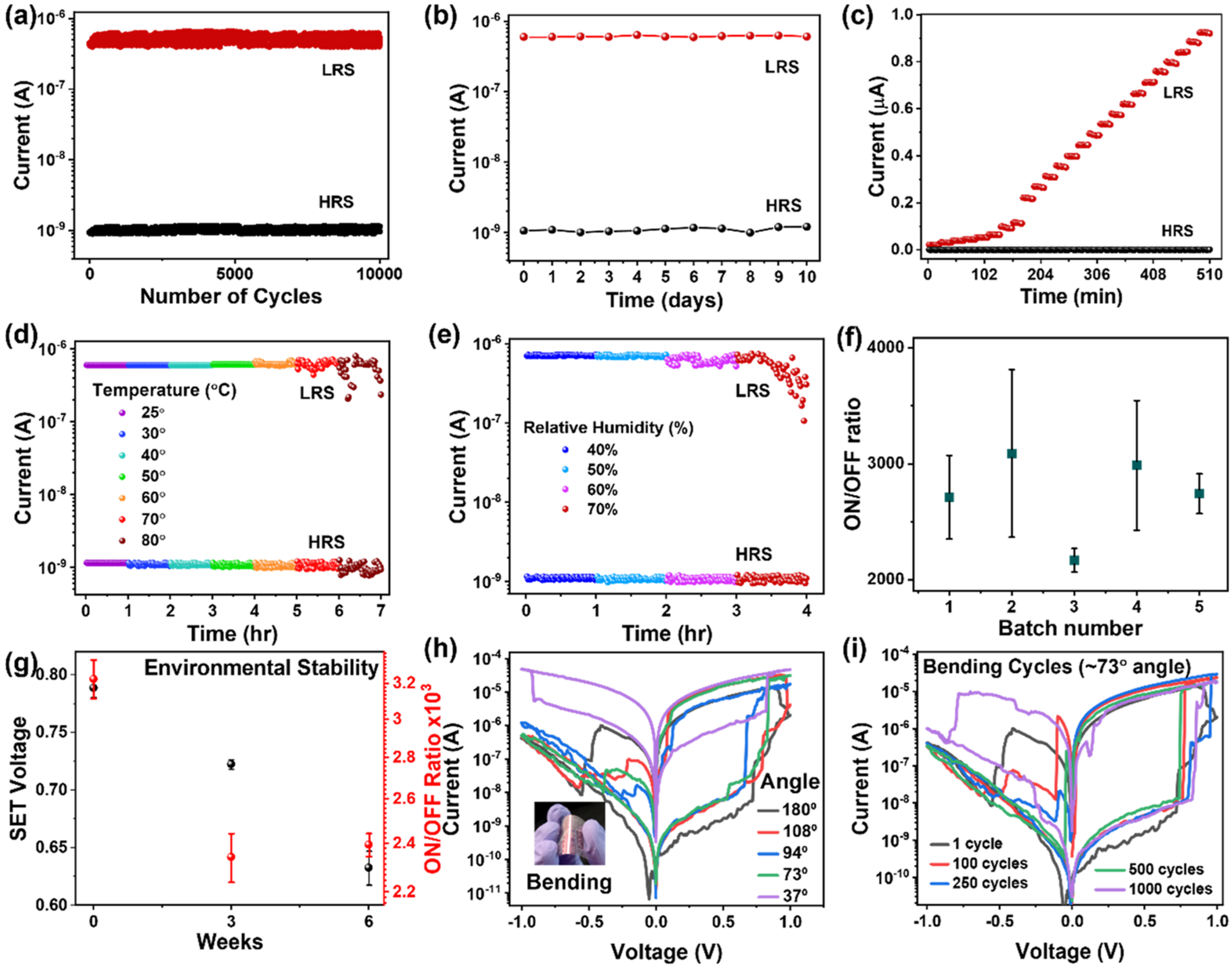


**Figure 4.** (a) Endurance for $10^4$ cycles. (b) Retention of $\sim 10^6$ s. (c) Multilevel retention of 25 states for 20 min ($\sim 10^3$ s). (d) Temperature-dependent retention at 25 (RT), 30, 40, 50, 60, 70, and 80 °C for $\sim 10^3$ s each. (e) Relative humidity-dependent retention at 40, 50, 60, and 70% for $\sim 10^3$ s each. (f) Batch-to-batch performance comparison of 50 devices per batch. (g) Environmental stability. (h) $I-V$ characteristics for different bending angles ($A$ = 180, 108, 94, 73, and 37°). (i) $I-V$ characteristics after a number of bending cycles at 73° angle (1, 100, 250, 500, and 1000 cycles).

**Table 1. Comparison between Switching Parameters for Different Active Materials**

| Sr. no. | Material | ON/OFF ratio | SET−RESET (V) | Endurance cycle | Retention (s) | Power Consumption | refs |
|---|---|---|---|---|---|---|---|
| 1 | p-$Ti_3C_2Tx$ MXene | $10^2$ | 0.72/−1.0 | $10^4$ | $10^6$ | 0.24 nJ | our work |
| 2 | $Mo_2C/MoS_2$ | $10^3$ | | $10^4$ | $>10^4$ | 0.16 mW | 39 |
| 3 | black phosphorus | $10^7$ | −2/1 | $10^2$ | $10^4$ | 4.5 fJ | 40 |
| 4 | $InO_x$ | 10 | | $10^2$ | $\sim 10^3$ | | 41 |
| 5 | $HfO_x$ | $10^2$ | 1.4/−2.85 | | $10^4$ | | 42 |
| 6 | parylene | $10^5$ | 2.5 | | $10^4$ | | 43 |
| 7 | PPX-C | 10 | 0.8/−0.4 | 300 | $10^4$ | | 44 |
| 8 | $HfSe_2$ | $10^2$ | 0.6/−0.8 | 500 | $10^4$ | 0.82 pJ | 45 |
| 9 | hBN/FLG | 480 | 0.66/−0.9 | 500 | $\sim 10^3$ | | 46 |
| 10 | $WS_2$ NSs: PMMA nanocomposite | $10^3$ | 0.6/−4.5 | 200 | $10^4$ | | 47 |
| 11 | $Cs_3Sb_2I_9$ (0D) | $10^2$ | 1/−1 | 500 | 5000 | | 48 |
| 12 | PPX | | 1.9/−1.9 | | | 3 nJ | 49 |
| 13 | Cu-TCNQ | $10^3$ | 3.5/0.4 | $10^3$ | | | 50 |
| 14 | parylene | 2.5/−3 | 104 | 120 | $10^4$ | 150 μW | 43 |
| 15 | nitride | $10^2$ | −1.5/0.2 | | | | 51 |

The invariant electrical performance measured up to the sixth week shows strong environmental stability (Figure 4g).[54] It should be noted that all of the devices were fabricated and measured in ambient conditions without any encapsulation



https://doi.org/10.1021/acsami.4c01364
ACS Appl. Mater. Interfaces 2024, 16, 17821−17831

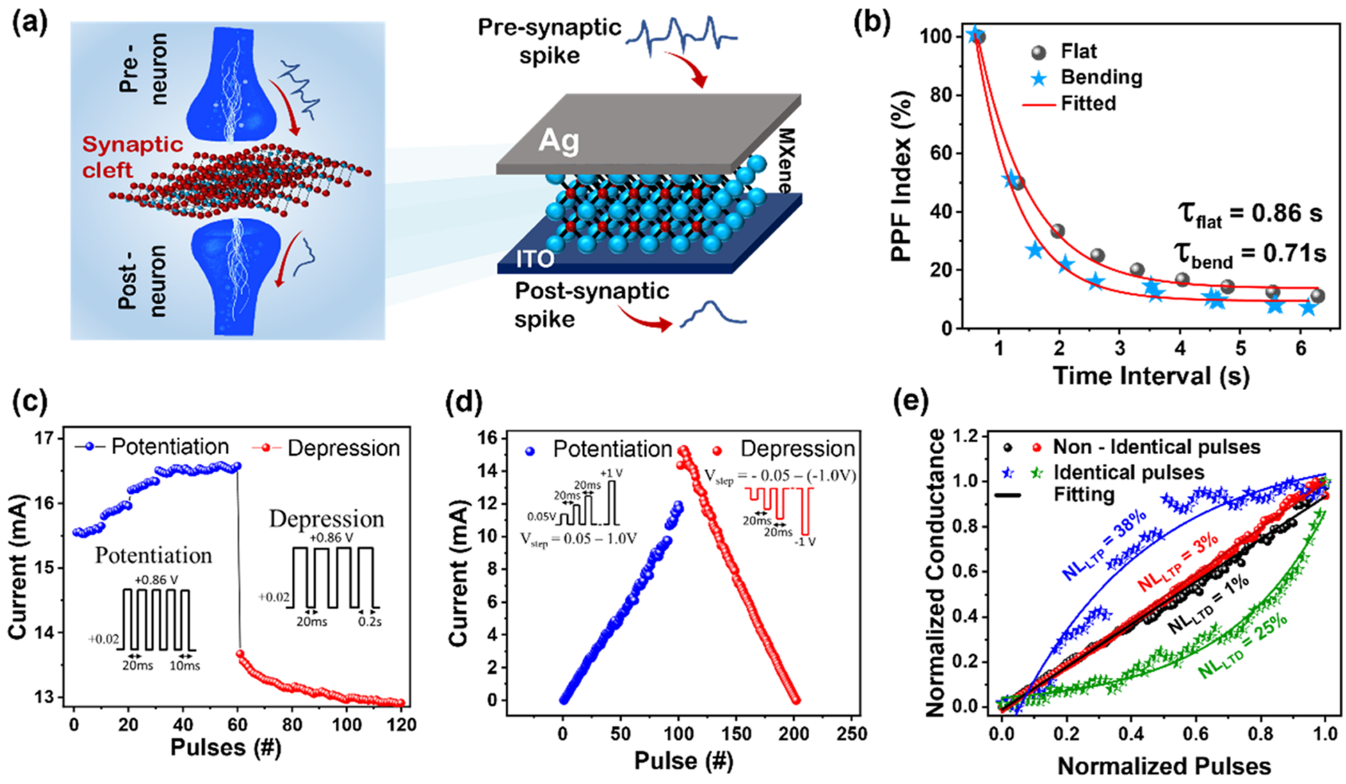


**Figure 5.** (a) Illustration of the 2D p-$Ti_3C_2T_x$ MXene-based memristor analogous to the biological synaptic connection. (b) PPF index in flat as well as bending condition (~73° angle). Potentiation and depression (P & D) in bending condition (~73° angle). (c) Identical pulse. (d) Nonidentical pulse. (e) Normalized P & D characteristics.

while being stored in a desiccator for a stability test. Over the period, the diffusion of Ag ions into the active layer makes the filament formation easier, and therefore a low SET voltage of 0.65 V on the sixth week is observed compared to 0.79 V on the zeroth week.

The presence of Al ions in MXene layers offers additional structural reinforcement in p-$Ti_3C_2T_x$, which contributes to a higher resistance against deformation or cracking when subjected to mechanical stress. The residual Al left in the MXene nanosheets adds additional stability by giving the hereditary environmental stability of the parent material MAX phase belonging to the ceramics family. Due to the resilience offered at the time of mechanical stress at different bending conditions (angles ~108°, 94°, 73°, and 37°), the RS is performed with invariant electrical performance bending up to 73° angle (Figure 4h). Further, to test the tolerance capability after various bending cycles at a 73° angle (1, 100, 250, 500, and 1000 cycles), the consistency resistive switching performance is demonstrated (Figure 4i). After 1000 bending cycles, the surface of the p-$Ti_3C_2T_x$ film on the PET substrate is verified by the SEM analysis, with no observable change in the morphology and emergence of any crack (Figure S6).

**2.3. Synaptic Performance.** The memristor mimics the analogous behavior of the biological synapse. Here, the top electrode, bottom electrode, and active layer act as pre-neuron, post-neuron, and synaptic cleft of the biologic synapse, respectively (Figure 5a). The neurotransmitters in pre-neurons are released as a result of the action potential generated by the calcium ion channels. These released neurotransmitters travel through the synaptic cleft and are received by the post-neuron terminal; thus, the information is transmitted from one neuron to another.[55] The synaptic connection between neurons undergoes both strengthening and weakening in response to repetitive firing. This ability of the synapse is known as synaptic plasticity. Herein, we demonstrate the synaptic characterizations of the PET/ITO/p-$Ti_3C_2T_x$/Ag device as an artificial synapse. When the continuous voltage sweeps of 0 V → +1 V → 0 V are applied, the current increases gradually (Figure S7a). Similarly, when continuous negative voltage sweeps are applied, the current decreases gradually in each cycle (SI, S7b). The change in the current magnitude indicates the basic implication for the existence of synaptic plasticity. Paired-pulse facilitation (PPF) is a form of short-term plasticity attributed to the replication of the synaptic plasticity observed in the human brain. The current ratio of >1 from two consecutive voltage pulses signifies the intensification of the facilitation of synaptic plasticity. In Figure 5b, the PPF index was calculated using the equation PPF index $= \left(\frac{A_2 - A_1}{A_1}\right) \times 100\%$ (where $A_1$ and $A_2$ are the currents of the first and second pulse, respectively) for the flat as well as maximum bending states (~73° angle).[56] PPF index is fitted by the exponential fitting curve equation $y = B_1 \times \exp\left(-\frac{x}{t_1}\right) + y_0$. Figure S7c (SI) shows the PPF at flat and bending conditions. The tuning of the pulse width from shorter to wider signifies the transition from short-term to long-term plasticity (Figure S7d).

Potentiation and depression (P & D) are other fundamental characteristics that represent the learning and forgetting behavior of the artificial synapse. At a maximum bending angle (~73°), the P & D of a p-$Ti_3C_2T_x$-based memristor with identical and nonidentical input stimuli was investigated. The identical voltage pulses of 0.86 V with 10 ms pulse width (20


https://doi.org/10.1021/acsami.4c01364
ACS Appl. Mater. Interfaces 2024, 16, 17821−17831

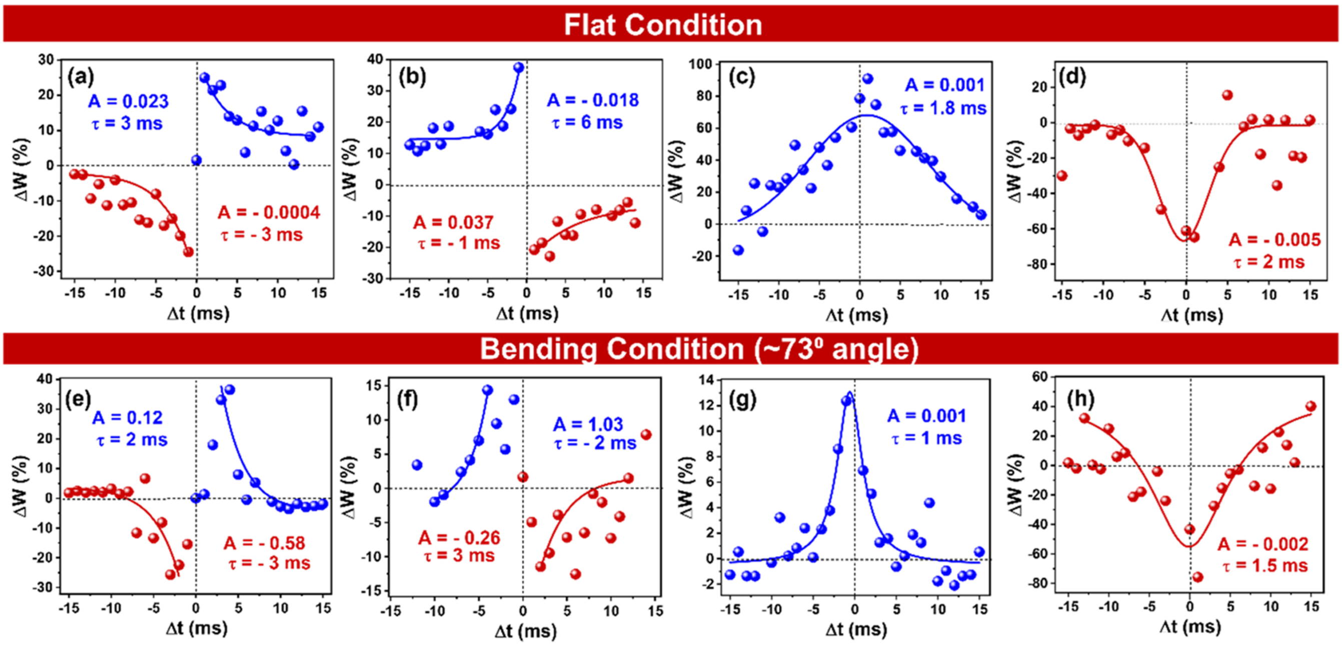


**Figure 6.** Spike time-dependent plasticity (STDP) characterization of 2D p-$Ti_3C_2T_x$ MXene-based memristor in flat and bending conditions (~73° angle), respectively. (a, e) Asymmetric Hebbian, (b, f) Asymmetric anti-Hebbian, (c, g) Symmetric Hebbian, and (d, h) Symmetric anti-Hebbian.

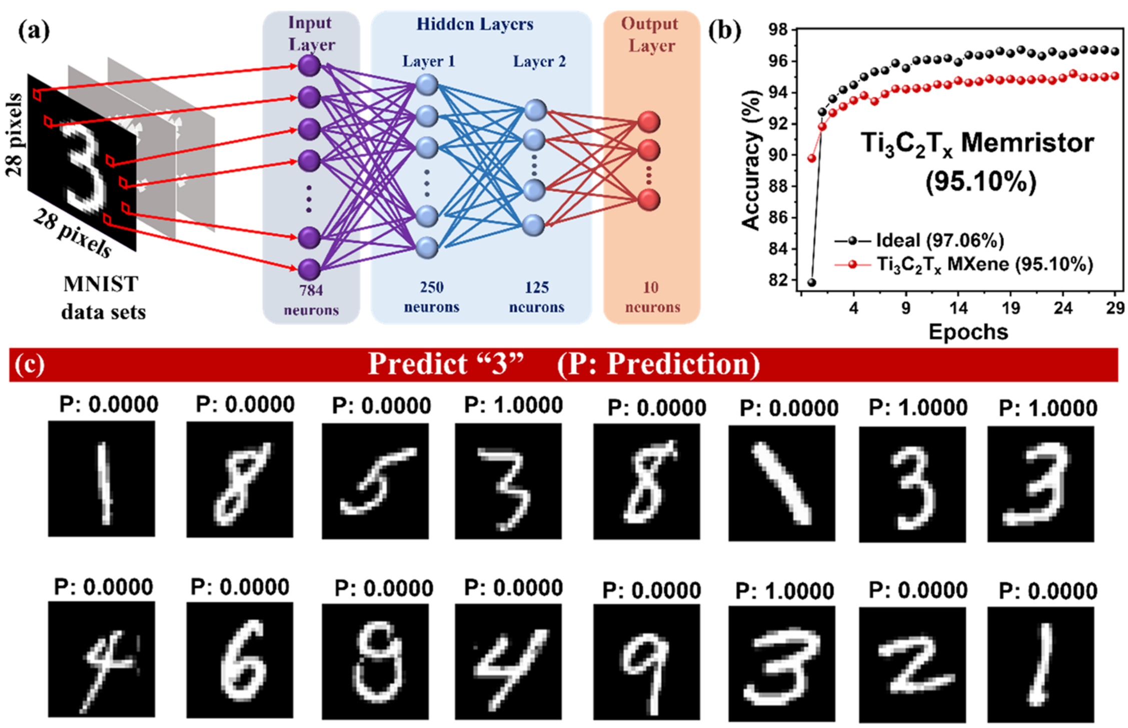


**Figure 7.** MNIST pattern recognition. (a) Illustration of the four-layer neural network for pattern recognition architecture. (b) Pattern recognition accuracy of the ideal synaptic device (97.06%) and of 2D p-$Ti_3C_2T_x$ MXene-based memristor synaptic device (95.10%) after 29 epochs. (c) Prediction accuracy test of the simulated ANN.

ms pulse duration) were applied (inset of Figure 5c) to obtain the potentiation, while devices show the depression characteristics with a higher pulse width of 200 ms (Figure 5c, for flat refer to SI, Figure S8a). Similarly, a nonidentical pulse applied for the potentiation consists of 0.05−1.0 V and the depression consists of −0.05 to −1.0 V with the same pulse width of 20 ms (Figure 5d, for flat, refer to SI, Figure S8b).

Ideally, normalized P & D conductance should be linear in behavior. The gradual increment in conductance and linearity are the basic requirements of an artificial neural network (ANN).[57] Therefore, it is important to minimize nonlinearity and asymmetry in order to maintain accurate weight values. The p-$Ti_3C_2T_x$-based memristor demonstrates a significant transition toward the decrease in nonlinearity when comparing identical pulses (38 and 25%) to nonidentical pulses (3 and


https://doi.org/10.1021/acsami.4c01364
ACS Appl. Mater. Interfaces 2024, 16, 17821−17831

1%) for potentiation and depression, respectively (Figure 5e). The nonlinearity effect is calculated using the equation $NL=\frac{\left[\frac{(G_{max}-G_{min})}{2}+G_{min}\right]-G_s}{\frac{(G_{max}-G_{min})}{2}+G_2}\times 100\%$. To demonstrate the mechanical stability, retention of P & D is measured up to $\sim 10^4$ pulsed cycles on flat conditions (see Figure S8c).

Furthermore, Hebbian learning rule-based spike time-dependent plasticity (STDP) is investigated to show the potential of these devices for neuromorphic applications. The Asymmetric Hebbian (Figure 6a,e), Asymmetric anti-Hebbian (Figure 6b,f), Symmetric Hebbian (Figure 6c,g), and symmetric anti-Hebbian (Figure 6d,h) based synaptic learning is mimicked by the p-$Ti_3C_2T_x$-based memristor in flat and bending conditions (~73° angle), respectively. These learning rules are based on the relative time difference ($\Delta t$) between the spikes employed at the pre- and post-synaptic neurons. When the post-synaptic spike follows the pre-synaptic spike ($\Delta t > 0$), the strengthening of the synaptic plasticity can be observed, which indicates the transition of the device into the long-term potentiated (LTP) state. While the pre-synaptic spike follows the post-synaptic spike ($\Delta t < 0$), the connection between the synapse weakens, and long-term depression (LTD) can be observed.[58] The spikes applied in this study can be found in the SI (Figure S9). The experimental data was fitted using the function $\Delta W = A \times \exp\left(-\frac{\Delta t}{\tau}\right) + \Delta W_0$ and the Gaussian function $\Delta W = A \times \exp\left(-\frac{\Delta t^2}{\tau^2}\right) + \Delta W_0$. The fastest biological synaptic transmission typically occurs within a time frame of ~1 ms. This refers to the speed at which signals are transmitted across the synapses in the nervous system. Herein, p-$Ti_3C_2T_x$-based flexible memristor devices demonstrate similar communication time (~3 ms) of the human brain and show the potential for the neuromorphic computing application.

The effectiveness of using a p-$Ti_3C_2T_x$-based memristor as an artificial synapse was assessed in a four-layer neural network designed for pattern recognition simulation. The neural network comprised an input layer with 784 neurons, two hidden layers with 250 and 125 neurons, respectively, and an output layer with 10 neurons, all interconnected by synapses (Figure 7a).[59] The input data for training and testing consisted of handwritten digits (ranging from 0 to 9) from the Modified National Institute of Standards and Technology (MNIST) database, with each digit represented by a 28 × 28 pixels image. The memristor's behavior, in terms of linearity, dynamic range, and precision during the potentiation and depression processes (Figure 4d), played a crucial role in updating the synaptic weights during the training phase. After the completion of 30 training epochs, the p-$Ti_3C_2T_x$-based memristor achieved an impressive recognition accuracy of 95.10% (Figure 7b). To benchmark its performance, the same neural network simulation was also conducted using an ideal synaptic device characterized by perfect linearity, an infinite dynamic range, and an infinite number of conductance states, achieving an accuracy of 97.07%. The comparison table of MNIST pattern recognition accuracies of other materials suggests that the accuracy of the p-$Ti_3C_2T_x$-based memristor shows state-of-the-art recognition at 29 epochs only (SI, Table S1). Prediction of the targeted number is done to showcase the potential of the device for image recognition (Figure 7c). The study suggests that further improvements and optimization in memristor technology could lead to even more competitive results in artificial synapse applications for future neuromorphic computing systems.

## 3. CONCLUSIONS

In summary, through a nontoxic, *in situ* HF route, $Ti_3C_2T_x$ has been partially synthesized and the $Ti_3C_2T_x$ MXene is used to fabricate the memristor. The fully etched $Ti_3C_2T_x$ (f-$Ti_3C_2T_x$)-based memristors can be used for data storage (~$10^3$ cycles) owing to stable endurance performance and data retention capabilities up to ~$10^2$ s. The p-$Ti_3C_2T_x$-based memristor shows tunable resistive switching phenomenon with a low operating voltage of 1.0 V. These memristor showcased excellent nonvolatile data storage properties, with a robust ~$10^3$ ON/OFF ratio, high endurance of ~$10^4$ cycles, multilevel resistance states, and long data retention measured up to ~$10^6$ s (10 days). High mechanical stability up to ~73° bending angle (after >1000 bending cycles) and environmental robustness are confirmed with consistence switching characteristics under increasing temperature and humid conditions. Furthermore, a p-$Ti_3C_2T_x$-based memristor was employed to mimic the biological synapse by performing paired-pulse facilitation (PPF), PPF index, potentiation and depression (P&D), spike time-dependent plasticity (STDP), and MNIST pattern recognition of ~95%. Also, the learning−forgetting pattern was measured for ~$10^4$ cycles as potentiation and depression. The synaptic characterizations were characterized for flat and bending conditions for flexible applications. This reveals that MXene can be a good candidate for flexible memory devices and neuromorphic computing.

## 4. EXPERIMENTAL SECTION

**4.1. Synthesis of p-$Ti_3C_2T_x$ MXene.** In a reaction vessel, 15 mL of 6 M hydrochloric acid, 0.8 g of lithium fluoride, and 0.75 g of $Ti_3AlC_2$ powder were combined with 2.5 mL of deionized water. In a 40 °C silicon oil bath, the reaction mixture was kept on magnetic stirring for 24 h. In 50 mL of deionized water, the etched MXene was centrifuged for 5 min at 3500 relative centrifugal force (RCF). The washing process was repeated five times, and the material was then filtered and vacuum-dried. The multilayer MXene $Ti_3C_2T_x$ powder preparation was finished at this point. The produced MXene powder was then dissolved at a concentration of 0.7 mg/mL in deionized water. The suspension was stirred for 30 min, sealed, and then sonicated in a bath sonicator for 30 min.

**4.2. Synthesis of f-$Ti_3C_2T_x$ MXene.** In a reaction vessel, 15 mL of 12 M hydrochloric acid, 1.2 g of lithium fluoride, and 0.75 g of $Ti_3AlC_2$ powder were combined with 2.5 mL of deionized water. In a 40 °C silicon oil bath, the reaction mixture was kept on magnetic stirring for 24 h. In 50 mL of deionized water, the etched MXene was centrifuged for 5 min at 3500 RCF. The washing process was repeated five times, and the material was then filtered and vacuum-dried. The multilayer MXene $Ti_3C_2T_x$ powder preparation was finished at this point. The produced MXene powder was then dissolved at a concentration of 0.7 mg/mL in deionized water. The suspension was stirred for 30 min, sealed, and then sonicated in a bath sonicator for 30 min.

**4.3. Fabrication of Device.** Spin-coating was used to fabricate a device with a simple sandwich structure. As a growth substrate, PET/ITO was used. The substrate was first chopped into 1.5 × 1.5 $cm^2$ squares and properly cleaned with a DI water−acetone solution. The spin-coating process was used to deposit the produced (p- and f-) $Ti_3C_2T_x$ MXene on the PET/ITO substrate; after deposition, it was annealed at 60 °C for 30 min. The resulting nanolayer had a thickness of about 150 nm. Finally, using a shadow mask, a top Ag electrode with a diameter of 0.1 mm was manually deposited. After that, it was dried in a vacuum chamber for 30 min to preserve it free from contaminants. The memristor device is now ready for testing and application.

**4.4. Characterizations.** SEM was conducted to investigate the morphology of the MXene nanosheets and the active layer MXene film thickness by cross-sectional FE-SEM by ZEISS Ultra 55. To investigate the synthesis of MXene nanosheets, XRD was done by X'Pert PRO. UV−vis spectroscopy was conducted to investigate the optical properties of the memristor device from SHIMADZU UV-1900i. Current−voltage sweep and voltage pulse measurements were performed using the source measurement unit (SMU) Keithley 2450 and 2604B in ambient conditions. An electrical module ArcONE was employed for STDP measurements.

## ASSOCIATED CONTENT

### Supporting Information

The Supporting Information is available free of charge at https://pubs.acs.org/doi/10.1021/acsami.4c01364.

FT-IR, UV, *I*−*V* fitting, *I*−*V* consecutive positive and negative pulses, PPF, STDP input spikes, and comparison table of MNIST accuracies (PDF)

## AUTHOR INFORMATION

### Corresponding Authors

**Ankur Solanki** − *Flextronics Lab and Department of Physics, School of Energy Technology, Pandit Deendayal Energy University, Gandhinagar 382426 Gujarat, India*; orcid.org/0000-0002-8305-8536; Email: Ankur.Solanki@sot.pdpu.ac.in

**Nitin Chaudhari** − *Advanced Hybrid Nanomaterial Laboratory, Department of Chemistry, School of Energy Technology, Pandit Deendayal Energy University, Gandhinagar 382426 Gujarat, India*; orcid.org/0000-0002-8324-577X; Email: Nitin.Chaudhari@sot.pdpu.ac.in

### Authors

**Jeny Gosai** − *Advanced Hybrid Nanomaterial Laboratory, Department of Chemistry, School of Energy Technology, Pandit Deendayal Energy University, Gandhinagar 382426 Gujarat, India; Flextronics Lab, Pandit Deendayal Energy University, Gandhinagar 382426 Gujarat, India*

**Mansi Patel** − *Flextronics Lab and Department of Physics, School of Energy Technology, Pandit Deendayal Energy University, Gandhinagar 382426 Gujarat, India*

**Lingli Liu** − *School of Physical and Mathematical Sciences, Nanyang Technological University, Singapore 637371, Singapore*; orcid.org/0000-0002-4360-2699

**Aziz Lokhandwala** − *Flextronics Lab and Department of Physics, School of Energy Technology, Pandit Deendayal Energy University, Gandhinagar 382426 Gujarat, India*

**Parth Thakkar** − *Flextronics Lab and Department of Physics, School of Energy Technology, Pandit Deendayal Energy University, Gandhinagar 382426 Gujarat, India*

**Mun Yin Chee** − *School of Physical and Mathematical Sciences, Nanyang Technological University, Singapore 637371, Singapore*; orcid.org/0000-0002-1580-1463

**Muskan Jain** − *Flextronics Lab and Department of Physics, School of Energy Technology, Pandit Deendayal Energy University, Gandhinagar 382426 Gujarat, India*

**Wen Siang Lew** − *School of Physical and Mathematical Sciences, Nanyang Technological University, Singapore 637371, Singapore*; orcid.org/0000-0002-5161-741X

Complete contact information is available at: https://pubs.acs.org/10.1021/acsami.4c01364

### Author Contributions

J.G. synthesized MXene, fabricated the device, performed the structural and electrical measurements, performed STDP, analyzed the data, and wrote the manuscript. M.P. performed the P & D, plotted and analyzed the data, and helped with the manuscript writing. L.L. performed the MNIST pattern recognition. P.T. performed the UV and FT-IR measurements. A.L. helped in the STDP data analysis and discussion. M.Y.C. wrote the code for MNIST pattern recognition. M.J. helped to analyze the *I*−*V* slope fitting and plotting. W.S.L. supervised the MNIST pattern recognition. N.C. supervised the synthesis and characterizations of MXene. A.S. supervised the device fabrication and characterizations of the memristor. All the authors reviewed the final manuscript.

### Notes

The authors declare no competing financial interest.

## ACKNOWLEDGMENTS

A.S. and J.G. gratefully acknowledge the fabrication support from the Science and Engineering Research Board (SERB) core research grant CRG/2020/000869. A.S. would also like to gratefully acknowledge the Gujarat Council on Science and Technology (GUJCOST) research grant GUJCOST/STI/2021-22/3873 from the government of Gujarat, India, to support electrical characterizations. N.C. would like to acknowledge financial support from Pandit Deendayal Energy University (PDEU) under the Start-up grant ORSP/R&D/PDPU/2021/NC00/R0069. Solar Research and Development Centre (SRDC) PDEU is also acknowledged for conducting FE-SEM and XRD measurements.

## ABBREVIATIONS

2D:two dimensional
Al:aluminum
ANN:artificial neural network
DI water:deionized water
DMSO:dimethyl sulfoxide
FE-SEM:field emission scanning electron microscopy
FT:IR:Fourier transformer infrared spectroscopy
f-$Ti_3C_2T_x$:fully etched $Ti_3C_2T_x$ MXene
HCL:hydrochloric acid
HF:hydrofluoric acid
ITO:indium tin oxide
LiF:lithium fluoride
LTD:long-term depression
LTP:long-term potentiation
P & D:potentiation and depression
PET:poly(ethylene terephthalate)
PPF:paired pulsed facilitation
p-$Ti_3C_2T_x$:partially etched $Ti_3C_2T_x$ MXene
RS:resistive switching
STDP:spike time-dependent plasticity
XRD:X-ray diffraction

## REFERENCES

(1) Yan, X.; Zhao, J.; Liu, S.; Zhou, Z.; Liu, Q.; Chen, J.; Liu, X. Y. Memristor with Ag-Cluster-Doped Tio2 Films as Artificial Synapse for Neuroinspired Computing. *Adv. Funct. Mater.* **2018**, *28* (1), No. 1705320, DOI: 10.1002/adfm.201705320.

(2) Strukov, D. B.; Snider, G. S.; Stewart, D. R.; Williams, R. S. The Missing Memristor Found. *Nature* **2008**, *453* (7191), 80−83.

(3) Ho, Y.; Huang, G. M.; Li, P. In *Nonvolatile Memristor Memory: Device Characteristics and Design Implications*, Proceedings of the 2009

International Conference on Computer-Aided Design; San Jose, California, 2009.
(4) Patel, M.; Kumbhar, D. D.; Gosai, J.; Sekhar, M. R.; Mallajosyula, A. T.; Solanki, A. Hybrid Perovskite-based Flexible and Stable Memristor by Complete Solution Process for Neuromorphic Computing. *Adv. Electron. Mater.* **2023**, *9* (4), No. 2200908.
(5) Patel, M.; Hemanth, N. R.; Gosai, J.; Mohili, R.; Solanki, A.; Roy, M.; Fang, B.; Chaudhari, N. K. MXenes: Promising 2d Memristor Materials for Neuromorphic Computing Components. *Trends Chem.* **2022**, *4* (9), 835−849.
(6) Mannocci, P.; Pedretti, G.; Giannone, E.; Melacarne, E.; Sun, Z.; Ielmini, D. A Universal, Analog, in-Memory Computing Primitive for Linear Algebra Using Memristors. *IEEE Trans. Circuits Syst.-I* **2021**, *68* (12), 4889−4899.
(7) Mehonic, A.; Sebastian, A.; Rajendran, B.; Simeone, O.; Vasilaki, E.; Kenyon, A. J. Memristors—from in-Memory Computing, Deep Learning Acceleration, and Spiking Neural Networks to the Future of Neuromorphic and Bio-Inspired Computing. *Adv. Intell. Syst.* **2020**, *2* (11), No. 2000085.
(8) Ryu, H.; Kim, S. Implementation of a Reservoir Computing System Using the Short-Term Effects of Pt/Hfo2/Taox/Tin Memristors with Self-Rectification. *Chaos, Solitons Fractals* **2021**, *150*, No. 111223.
(9) Voglis, G.; Tavernarakis, N. The Role of Synaptic Ion Channels in Synaptic Plasticity. *EMBO Rep.* **2006**, *7* (11), 1104−1110.
(10) Huh, W.; Lee, D.; Lee, C.-H. Memristors based on 2d Materials as an Artificial Synapse for Neuromorphic Electronics. *Adv. Mater.* **2020**, *32* (51), No. 2002092.
(11) Thakkar, P.; Gosai, J.; Gogoi, H. J.; Solanki, A. From Fundamentals to Frontiers: A Review of Memristor Mechanisms, Modeling and Emerging Applications. *J. Mater. Chem. C* **2024**, *12*, 1583.
(12) Mahata, C.; Ismail, M.; Kang, M.; Kim, S. Synaptic Plasticity and Quantized Conductance States in Tin-Nanoparticles-based Memristor for Neuromorphic System. *Nanoscale Res. Lett.* **2022**, *17* (1), No. 58, DOI: 10.1186/s11671-022-03696-2.
(13) Gautam, M. K.; Kumar, S.; Chaudhary, S.; Hindoliya, L. K.; Kumbhar, D. D.; Park, J. H.; Htay, M. T.; Mukherjee, S. Experimental Validation of Switching Dependence of Nanoscale $Y_2O_3$ Memristors on Electrode Symmetry Via Physical Electrothermal Modeling. *ACS Appl. Electron. Mater.* **2023**, *5*, 3885.
(14) Kumar, S.; Kumbhar, D. D.; Park, J. H.; Kamat, R. K.; Dongale, T. D.; Mukherjee, S. $Y_2O_3$-based Crossbar Array for Analog and Neuromorphic Computation. *IEEE Trans. Electron Devices* **2023**, *70* (2), 473−477.
(15) Kumbhar, D. D.; Je, Y.; Hong, S.; Lee, D.; Kim, H.; Kwon, M. J.; Cho, S.-Y.; Lee, D.-H.; Lim, D.-H.; Kim, S. et al. Molecularly Reconfigurable Neuroplasticity of Layered Artificial Synapse Electronics *Adv. Funct. Mater.*, *1* 2311994 DOI: 10.1002/adfm.202311994.
(16) Betal, A.; Bera, J.; Sahu, S. Non-Volatile Memristor-based Artificial Synaptic Behavior of Redox-Active Organic Composites. *J. Mater. Chem. C* **2023**, *11* (14), 4674−4682.
(17) Gogoi, H. J.; Bajpai, K.; Mallajosyula, A. T.; Solanki, A. Advances in Flexible Memristors with Hybrid Perovskites. *J. Phys. Chem. Lett.* **2021**, *12* (36), 8798−8825.
(18) Khemnani, M.; Tripathi, B.; Thakkar, P.; Gosai, J.; Jain, M.; Chandra, P.; Solanki, A. Investigating the Role of Interfacial Layer for Resistive Switching in a Hybrid Dion-Jacobson Perovskite-based Memristor. *ACS Appl. Electron. Mater.* **2023**, *5* (9), 5249−5256.
(19) Patel, M.; Gosai, J.; Lokhandwala, A.; Solanki, A. Slow Migration-Controlled Resistive Switching in Stable Dion−Jacobson Hybrid Perovskites for Flexible Memristive Applications. *ACS Appl. Electron. Mater.* **2024**, *6* (1), 587−598.
(20) Jain, M.; Patel, M. J.; Liu, L.; Gosai, J.; Gogoi, H. J.; Khemnani, M.; Chee, M. Y.; Guerrero, A.; Lew, W. S.; Solanki, A. Insights into Synaptic Functionality and Resistive Switching in Lead Iodide Flexible Memristor Devices. *Nanoscale Horiz.* **2024**, *9*, No. 438, DOI: 10.1039/D3NH00505D.
(21) Lokhandwala, A.; Thakkar, P.; Gosai, J.; Oza, S.; Solanki, A. Unlocking the Resistive Switching in Acacia Senegal-based Electrolyte for Neuromorphic Computation. *J. Mater. Chem. C* **2024**, *12*, 2173.
(22) Luo, Z.-D.; Peters, J. J. P.; Sanchez, A. M.; Alexe, M. Flexible Memristors based on Single-Crystalline Ferroelectric Tunnel Junctions. *ACS Appl. Mater. Interfaces* **2019**, *11* (26), 23313−23319.
(23) Xia, Q.; Yang, J. J. Memristive Crossbar Arrays for Brain-Inspired Computing. *Nat. Mater.* **2019**, *18* (4), 309−323.
(24) Gogotsi, Y.; Anasori, B. The Rise of MXenes. *ACS Nano* **2019**, *13* (8), 8491−8494.
(25) Khot, A. C.; Dongale, T. D.; Park, J. H.; Kesavan, A. V.; Kim, T. G. $Ti_3C_2$-based MXene Oxide Nanosheets for Resistive Memory and Synaptic Learning Applications. *ACS Appl. Mater. Interfaces* **2021**, *13* (4), 5216−5227.
(26) Lim, K. R. G.; Shekhirev, M.; Wyatt, B. C.; Anasori, B.; Gogotsi, Y.; Seh, Z. W. Fundamentals of MXene Synthesis. *Nat. Synth.* **2022**, *1* (8), 601−614.
(27) Zhao, T.; Liu, H.; Yuan, L.; Tian, X.; Xue, X.; Li, T.; Yin, L.; Zhang, J. A Multi-Responsive MXene-based Actuator with Integrated Sensing Function. *Adv. Mater. Interfaces* **2022**, *9* (10), No. 2101948.
(28) Quan, W.; Shi, J.; Luo, H.; Fan, C.; Lv, W.; Chen, X.; Zeng, M.; Yang, J.; Hu, N.; Su, Y.; et al. Fully Flexible MXene-based Gas Sensor on Paper for Highly Sensitive Room-Temperature Nitrogen Dioxide Detection. *ACS Sens.* **2023**, *8* (1), 103−113.
(29) Han, M.; Shuck, C. E.; Rakhmanov, R.; Parchment, D.; Anasori, B.; Koo, C. M.; Friedman, G.; Gogotsi, Y. Beyond Ti3c2tx: MXenes for Electromagnetic Interference Shielding. *ACS Nano* **2020**, *14* (4), 5008−5016.
(30) Ma, R.; Zhang, X.; Zhuo, J.; Cao, L.; Song, Y.; Yin, Y.; Wang, X.; Yang, G.; Yi, F. Self-Supporting, Binder-Free, and Flexible $Ti_3C_2T_x$ MXene-based Supercapacitor Electrode with Improved Electrochemical Performance. *ACS Nano* **2022**, *16* (6), 9713−9727.
(31) Rao, D.; Zhang, L.; Wang, Y.; Meng, Z.; Qian, X.; Liu, J.; Shen, X.; Qiao, G.; Lu, R. Mechanism on the Improved Performance of Lithium Sulfur Batteries with MXene-based Additives. *J. Phys. Chem. C* **2017**, *121* (21), 11047−11054.
(32) Cao, S.; Chen, H.; Hu, Y.; Li, J.; Yang, C.; Chen, Z.; Wei, S.; Liu, S.; Wang, Z.; Sun, D.; Lu, X. MXene-based Single Atom Catalysts for Efficient Co2rr Towards Co: A Novel Strategy for High-Throughput Catalyst Design and Screening. *J. Chem. Eng.* **2023**, *461*, No. 141936.
(33) Yang, L.; Kan, D.; Dall'Agnese, C.; Dall'Agnese, C.; Dall'Agnese, Y.; Dall'Agnese, Y.; Wang, B.; Jena, A. K.; Wei, Y.; Chen, G.; Wang, X.-F.; Gogotsi, Y. Performance Improvement of MXene-based Perovskite Solar Cells Upon Property Transition from Metallic to Semiconductive by Oxidation of Ti3c2tx in Air. *J. Mater. Chem. A* **2021**, *9* (8), 5016−5025.
(34) Li, H.; Fan, R.; Zou, B.; Yan, J.; Shi, Q.; Guo, G. Roles of MXenes in Biomedical Applications: Recent Developments and Prospects. *J. Nanobiotechnol.* **2023**, *21* (1), No. 73, DOI: 10.1186/s12951-023-01809-2.
(35) Li, X.; Huang, Z.; Shuck, C. E.; Liang, G.; Gogotsi, Y.; Zhi, C. MXene Chemistry, Electrochemistry and Energy Storage Applications. *Nat. Rev. Chem.* **2022**, *6* (6), 389−404.
(36) Cao, Q.; Lü, W.; Wang, X. R.; Guan, X.; Wang, L.; Yan, S.; Wu, T.; Wang, X. Nonvolatile Multistates Memories for High-Density Data Storage. *ACS Appl. Mater. Interfaces* **2020**, *12* (38), 42449−42471.
(37) Luo, J.; Zhang, W.; Yuan, H.; Jin, C.; Zhang, L.; Huang, H.; Liang, C.; Xia, Y.; Zhang, J.; Gan, Y.; Tao, X. Pillared Structure Design of MXene with Ultralarge Interlayer Spacing for High-Performance Lithium-Ion Capacitors. *ACS Nano* **2017**, *11* (3), 2459−2469.
(38) Tang, M.; Li, J.; Wang, Y.; Han, W.; Xu, S.; Lu, M.; Zhang, W.; Li, H. Surface Terminations of MXene: Synthesis, Characterization, and Properties. *Symmetry* **2022**, *14*, No. 2232, DOI: 10.3390/sym14112232.
(39) Tang, X.; Yang, L.; Huang, J.; Chen, W.; Li, B.; Yang, S.; Yang, R.; Zeng, Z.; Tang, Z.; Gui, X. Controlling Sulfurization of 2d $Mo_2C$

Crystal for $Mo_2C/MoS_2$-based Memristor and Artificial Synapse. *npj Flexible Electron.* **2022**, *6* (1), No. 93, DOI: 10.1038/s41528-022-00227-y.

(40) Kumar, A.; Viscardi, L.; Faella, E.; Giubileo, F.; Intonti, K.; Pelella, A.; Sleziona, S.; Kharsah, O.; Schleberger, M.; Di Bartolomeo, A. Temperature Dependent Black Phosphorus Transistor and Memory. *Nano Express* **2023**, *4* (1), No. 014001.

(41) Huang, C.-H.; Weng, C.-Y.; Chen, K.-H.; Chou, Y.; Wu, T.-L.; Chou, Y.-C. Multiple-State Nonvolatile Memory based on Ultrathin Indium Oxide Film Via Liquid Metal Printing. *ACS Appl. Mater. Interfaces* **2023**, *15* (21), 25838−25848.

(42) Paul, A. D.; Biswas, S.; Das, P.; Edwards, H.; Dhanak, V.; Mahapatra, R. Effect of Aluminum Doping on Performance of $Hfo_x$-Based Flexible Resistive Memory Devices. *IEEE Trans. Electron Devices* **2020**, *67* (10), 4222−4227.

(43) Chen, Q.; Lin, M.; Wang, Z.; Zhao, X.; Cai, Y.; Liu, Q.; Fang, Y.; Yang, Y.; He, M.; Huang, R. Low Power Parylene-based Memristors with a Graphene Barrier Layer for Flexible Electronics Applications. *Adv. Electron. Mater.* **2019**, *5* (9), No. 1800852.

(44) Kim, J.-E.; Kim, B.; Kwon, H. T.; Kim, J.; Kim, K.; Park, D.-W.; Kim, Y. Flexible Parylene C-based Rram Array for Neuromorphic Applications. *IEEE Access* **2022**, *10*, 109760−109767.

(45) Li, S.; Pam, M. E.; Li, Y.; Chen, L.; Chien, y.-C.; Fong, X.; Chi, D.; Ang, K.-W. Wafer-Scale 2D Hafnium Diselenide based Memristor Crossbar Array for Energy-Efficient Neural Network Hardware. *Adv. Mater.* **2022**, *34* (25), No. 2103376.

(46) Qian, K.; Tay, R. Y.; Lin, M.-F.; Chen, J.; Li, H.; Lin, J.; Wang, J.; Cai, G.; Nguyen, V. C.; Teo, E. H. T.; Chen, T.; Lee, P. S. Direct Observation of Indium Conductive Filaments in Transparent, Flexible, and Transferable Resistive Switching Memory. *ACS Nano* **2017**, *11* (2), 1712−1718, DOI: 10.1021/acsnano.6b07577.

(47) Lee, J. H.; Wu, C.; Sung, S.; An, H.; Kim, T. W. Highly Flexible and Stable Resistive Switching Devices based on $WS_2$ Nanosheets: Poly (Methylmethacrylate) Nanocomposites. *Sci. Rep.* **2019**, *9* (1), No. 19316, DOI: 10.1038/s41598-019-55637-2.

(48) Park, Y.; Kim, S. H.; Lee, D.; Lee, J.-S. Designing Zero-Dimensional Dimer-Type All-Inorganic Perovskites for Ultra-Fast Switching Memory. *Nat. Commun.* **2021**, *12* (1), No. 3527.

(49) Matsukatova, A.; Minnekhanov, A.; Rylkov, V.; Demin, V.; Emelyanov, A. Resistive Switching Kinetics of Parylene-based Memristive Devices with Cu Active Electrodes. *J. Phys.: Conf. Ser.* **2021**, *1758*, No. 012025, DOI: 10.1088/1742-6596/1758/1/012025.

(50) Basori, R.; Kumar, M.; Raychaudhuri, A. K. Sustained Resistive Switching in a Single Cu:7,7,8,8-Tetracyanoquinodimethane Nanowire: A Promising Material for Resistive Random Access Memory. *Sci. Rep.* **2016**, *6* (1), No. 26764.

(51) Kim, S. J.; Kim, S. B.; Jang, H. W. Competing Memristors for Brain-Inspired Computing. *iScience* **2021**, *24* (1), No. 101889.

(52) Liu, N.; Li, Q.; Wan, H.; Chang, L.; Wang, H.; Fang, J.; Ding, T.; Wen, Q.; Zhou, L.; Xiao, X. High-Temperature Stability in Air of $Ti_3C_2T_x$ MXene-based Composite with Extracted Bentonite. *Nat. Commun.* **2022**, *13* (1), No. 5551.

(53) Zhao, X.; Wang, L.-Y.; Tang, C.-Y.; Zha, X.-J.; Liu, Y.; Su, B.-H.; Ke, K.; Bao, R.-Y.; Yang, M.-B.; Yang, W. Smart $Ti_3C_2T_x$ MXene Fabric with Fast Humidity Response and Joule Heating for Healthcare and Medical Therapy Applications. *ACS Nano* **2020**, *14* (7), 8793−8805.

(54) Zhang, J.; Li, S.; Hu, S.; Zhou, Y. Chemical Stability of $Ti_3C_2$ MXene with Al in the Temperature Range 500-700 °C. *Materials* **2018**, *11* (10), No. 1979, DOI: 10.3390/ma11101979.

(55) Erreger, K.; Matthies, H. J. G.; Galli, A.; Saunders, C. Neurotransmitter Transporters. In *Encyclopedia of Biological Chemistry*; Lennarz, W. J.; Lane, M. D., Eds.; Academic Press, 2013; pp 238−240.

(56) Hu, S. G.; Liu, Y.; Chen, T. P.; Liu, Z.; Yu, Q.; Deng, L. J.; Yin, Y.; Hosaka, S. Emulating the Paired-Pulse Facilitation of a Biological Synapse with a Niox-based Memristor. *Appl. Phys. Lett.* **2013**, *102* (18), No. 183510, DOI: 10.1063/1.4804374.

(57) Choi, H.-S.; Lee, Y.-J.; Park, H.; Cho, W.-J. Biocompatible Potato-Starch Electrolyte-based Coplanar Gate-Type Artificial Synaptic Transistors on Paper Substrates. *Int. J. Mol. Sci.* **2022**, *23* (24), No. 15901, DOI: 10.3390/ijms232415901.

(58) Li, Y.; Zhong, Y.; Zhang, J.; Xu, L.; Wang, Q.; Sun, H.; Tong, H.; Cheng, X.; Miao, X. Activity-Dependent Synaptic Plasticity of a Chalcogenide Electronic Synapse for Neuromorphic Systems. *Sci. Rep.* **2014**, *4* (1), No. 4906.

(59) Liu, L.; Dananjaya, P. A.; Chee, M. Y.; Lim, G. J.; Lee, C. X. X.; Lew, W. S. Proton-Assisted Redox-based Three-Terminal Memristor for Synaptic Device Applications. *ACS Appl. Mater. Interfaces* **2023**, *15* (24), 29287−29296.